

Numerical study of Valence Band states evolution in $\text{Al}_x\text{Ga}_{1-x}\text{As}$ [111] QDs systems

M. Lazarev¹

¹ *Department of Computer Science, LAMBDA, National Research University Higher School of Economics (HSE), Russia*

Corresponding Author:

Mikhail Lazarev¹

Pokrovsky Blvd, 11, Moscow, 109028

Email address: mvlazarev@hse.ru

Abstract

Quantum Dots (QDs) are very attractive nanostructures from an application point of view due to their unique optical properties. Optical properties and Valence Band (VB) states character was numerically investigated from the effect of nanostructure geometry and composition. Numerical simulation was carried out using Luttinger–Kohn model adapted to the particular use case of QDs in inverted pyramids. We present the source code of the 4-band Luttinger–Kohn model that can be used to model AlGaAs or InGaAs nanostructures. Here we focus on the optical properties study of GaAs/AlGaAs [111] QDs and Quantum Dot Molecules (QDMs). We examine the dependence of Ground State (GS) optical properties on their structural parameters and predict optimal parameters of the QD/QDM systems to achieve the dynamic control of GS polarization by the applied electric field.

1. Introduction

Low-dimensional nanostructures have unique optical characteristics influenced by geometry and composition. Nanostructures found a wide range of applications, for example, in solar cells [1], LEDs [2], lasers [3], and so on [4]. Dimensionality plays a curtail role in light-matter interaction and charges carrier's properties, thus the optical properties of the nanostructure. In Quantum Wells (QWs), light emission happens due to the recombination of electrons with heavy holes [5] in opposition to Quantum Wires (QWRs), where electrons recombine with light holes [6]. This difference has an impact on emitted light polarization. QDs are proven sources of single photons and are considered for integration in integrated quantum photonic circuits [7][8][9].

QDs have a complex spectral structure where carrier states can be as heavy and light. Previously has been shown that the hole character (heavy or light) in the Valence Band (VB) can be modified in a variety of nanostructures [10][11][12] by QD structure and material composition. Also, there are a few ways to achieve dynamic control over QD optical properties, such as the application of external electromagnetic fields [13][14] and strain [15]. Several groups have demonstrated electrically driven position control of QD in photonic crystals [16] and cavity and polarization control in micropillar cavities [17][18]. Also, wavelength emission control by

applying additional stress [19] has been demonstrated. The study of dynamic control over QD band structure is fundamental for novel functional materials and devices in a wide range of applications.

QD band structure can be calculated by several different methods *ab initio* [20][21], empirical pseudopotential method [22], and [23] etc. They require lots of computation time and power, making them impractical to simulate heterostructure electronic structures. On the other hand, the **kp** methods are widely applied to describe III–V semiconductor heterostructures' optical properties. Application of 4-band and 6-band Luttinger–Kohn **kp** models for (111)-oriented systems were introduced in [24][25] [26][27]. There are even higher dimensional models, 8-band [28][29], 10-band [30], and even 30-band models[31], but no source code with data to verify the findings. A larger model gives more accurate predictions, allowing us to consider more accurate effects like a decrease of optical gain for InGaAs/GaAs QWs with an increase in the hydrostatic pressure [32] (10-band vs 8-band). However, the needed accuracy depends on the application and experimental setup. Here to describe nanostructure VB properties, we use a relatively simple 4-band **kp** model implemented in the code, which agrees with experimental data obtained in previous studies. The 4-band **kp** model is a fast solution that well describes the VB structure. The detailed model description is presented in Section 2 of this article. Here we theoretically study the transition process between Light and Heavy holes like VB ground state (GS) characters in QDs of different geometries. We use the same modeling approach as in [33][34][35].

As a structure to model, we study QDs grown in inverted pyramids [36][37]. Nanostructures in inverted pyramids are well studied experimentally and demonstrate the ability to control the structure composition and geometry with high precision during material deposition. The MOVPE growth technique allows the growing of all possible varieties of nanostructures by controlling heterostructure composition along the growth direction. The schematic structure illustrations are presented in Figure 1. Each nanostructure in Figure 1 represents a nanostructure type that has been experimentally fabricated and reported in the literature; it is QWRs (Figure 1 a) [38], QDs (Figure 1 b) [12], tailored QDs [35][39][38] (Figure 1 e), Quantum Dot Molecules (QDMs) [33] (Figure 1 d) Dot-in-Dot (DiD) [34] (Figure 1 c). Different colors correspond to Al content in the structure in Figure 1 (a), schematically presented QWR (symmetry center) in an inverted pyramid. Due to the physical processes of nanostructure growth, QWR formation is always accompanied by the formation of side nanostructures QWs. In Figure 1 (a), such side nanostructures are colored green for Vertical QW and blue for Vicinal QWs colors. Summarily to QWR, the QD also forms its side nanostructures, Lateral QWRs. Thus, QD formation in QWR is presented in Figure 1 (b). Tailoring of Al content during the growth allows to realize in solid all possible nanostructures. In this study, we consider the central QWR region. In earlier work [12], pyramidal $\text{Al}_x\text{Ga}_{1-x}\text{As}$ QDs with heights of 10-100 nm were realized, and as it was reported by changing the QD size, it's possible to control polarization properties. But in [12], little attention was paid to the related VB states structure.

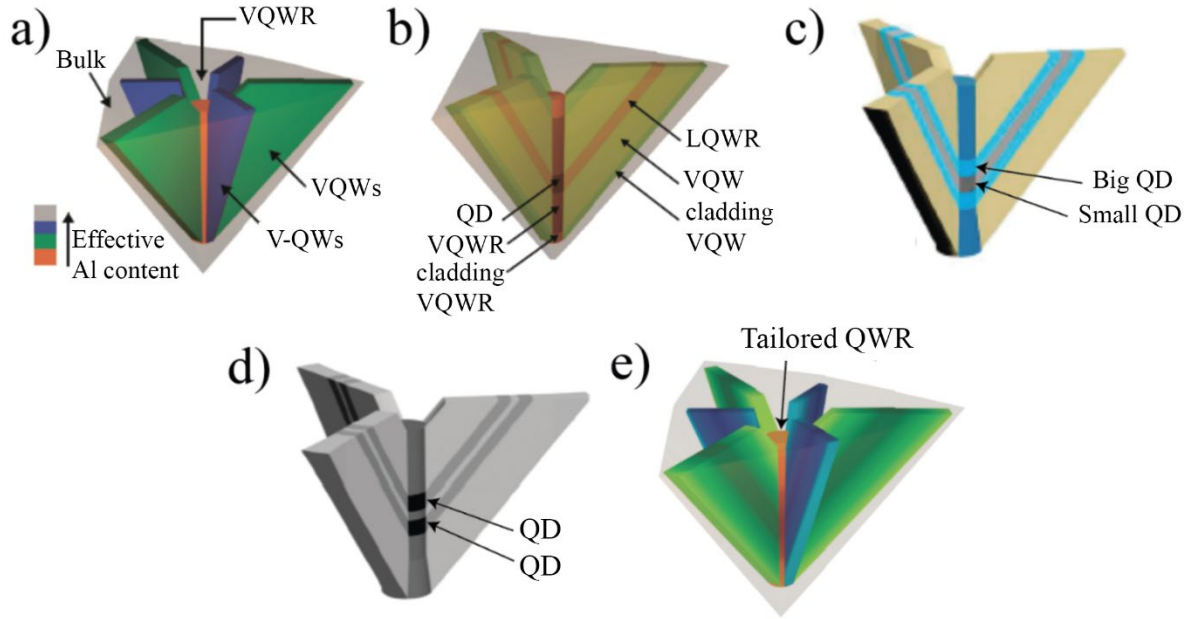


Figure 1. Schematic illustration of different kinds of AlGaAs nanostructures embedded in inverted pyramids. (a) “Long” quantum wire (QWR) laterally bounded by “vertical” QWs, (b) Quantum Dot, and (c) QD-in-QD heterostructure. (d) QDM of two coupled QDs. (e) Tailored potential QWR/QD. The color codes scale the Al mole fraction in the different parties of the heterostructures.

Achievement of dynamic control over light polarization emitted by the nanostructures in the inverted pyramid is also possible. Dynamic control of the GS emission polarization of quantum Dot in Dot (DiD) pyramidal nanostructure was proposed in [40]. However, the study used geometrical assumptions of the nanostructure that do not match experimental results, and the source code is not available. In [41] polarization optical properties of DiD in magnetic field study were reported, but polarization switching requires high magnetic field intensities and hence is not feasible for applications.

In this paper, we theoretically study VB GSs evolution in pyramidal QD/QDM systems from its geometry and material composition that forms the potential profile. The paper is divided into a few parts; in Section 2 introduces the simulation method (subsection 2.1) and approximations that we use for structure design (subsection 2.2). Section 3 is dedicated to simulation results; in subsection 3.1, we present single QD simulation results of GS VB evolution from its length and electric field. In subsection 3.2, we study QDM system evolution. In section 4, we conclude your findings. The Appendix contains the 4x4 Luttinger Hamiltonian derivation used in this study.

2. Method

2.1 Theory

Here we introduce the model with assumptions we used and implemented in the code [42]. As a basis, we start with the so-called mean field (Hartree-Fock) approximation. The result is a mean-field Hamiltonian for single electrons:

$$H = \frac{p^2}{2m_0} + V(r) + H_{SO} \text{ where } V(r) \text{ is the mean-field potential, spin-orbit interaction term}$$

$$H_{SO} = \frac{\hbar}{4m_0^2c^2} \sigma \cdot [\nabla V \times p] \text{ and } m_0 \text{ is the electron mass.}$$

Exploiting the lattice periodicity, we first look for solutions in the form of Bloch waves:

$$\psi_k^{(n)}(r) = u_k^{(n)}(r)e^{ikr}, \quad u_k^{(n)}(r) = u_k^{(n)}(r+a)$$

Substituting the Bloch wave function into the Hamiltonian and neglecting parts with fast oscillations we get [43]: $H = H^{k \cdot p} + H_{SO}$, where $H^{k \cdot p} = \left[\frac{p^2}{2m_0} + V(r) \right] + \left[\frac{\hbar}{m_0} k \cdot p + \frac{\hbar^2 k^2}{2m_0} \right]$, thus the Schrödinger equation looks like:

$$\left(\left[\frac{p^2}{2m_0} + V(r) \right] + \left[\frac{\hbar}{m_0} k \cdot p + \frac{\hbar^2 k^2}{2m_0} \right] + \frac{\hbar}{4m_0^2c^2} \sigma \cdot [\nabla V \times (p + \hbar k)] \right) u_k^{(n)}(r) = \varepsilon_k^{(n)} u_k^{(n)}(r)$$

Where σ are Pauli matrices, ∇V the gradient of atomic mean field potential. Our model works with this Hamiltonian and solves it in a 4-bands (S and P orbitals) approximation. To take into account infinite number of other bands Löwdin perturbation theory [27] was implied. See the supplementary material in Appendix for more details.

To each pair of electron and hole corresponds exciton energy and definer as follows:

$$E_X = E_g + E_{cb} + E_{vb} - E_{Coulomb}^{e-h}$$

Where E_{cb} , E_{vb} are the state energies in CB and VB, and $E_{Coulomb}^{e-h}$ is Coulomb interaction energy. These values depend on QD geometry and material composition. Usually, in small QDs confinement energy is strong compared to the Coulomb interaction. The Coulomb interaction in the case of strong confinement can be considered as a perturbation [44]. The perturbation to the Hamiltonian is then written as:

$$E_{Coulomb}^{e-h} = \iint \psi_{cb} \psi_{vb} \frac{e^2}{4\pi\epsilon_0\epsilon |r_{cb} - r_{vb}|} \psi_{cb}^* \psi_{vb}^* dr_{cb} dr_{vb}$$

where ψ_{vb} , ψ_{cb} are the valence and conduction band wavefunctions, r_{cb} , r_{vb} the electron and hole positions.

Observed light intensity and polarization dependence proportional to dipole moment matrix element [45]:

$$I_{eh} = \sum_{S_z = \pm \frac{1}{2}} \left| \sum_{J_z = \pm \frac{3}{2}, \pm \frac{1}{2}} \langle \phi_e^{S_z}(r) | \phi_h^{J_z}(r) \rangle \langle u_e^{S_z} | \mathbf{e} \cdot \mathbf{p} | u_h^{J_z} \rangle \right|^2$$

Where \mathbf{e} is polarization, \mathbf{p} is the momentum operator and \mathbf{u} is Bloch wavefunction. The identical polarization dependence corresponds to photon from electron-hole recombination in exciton. The final expression for polarization dependence in the case of orthogonal LH and HH wavefunctions along and perpendicular z direction is:

$$I_z \propto \left(\frac{4}{3} \langle \varphi_e | \varphi_{LH} \rangle^2 \right) I_{xy} \propto \left(\langle \varphi_e | \varphi_{HH} \rangle^2 + \frac{1}{3} \langle \varphi_e | \varphi_{LH} \rangle^2 \right)$$

Spectral measurements often use the degree of linear polarization (DOLP) value. Here we define DOLP as $DOLP = \frac{I_z - I_{xy}}{I_z + I_{xy}}$. For VB states with pure HH character, this yields

$DOLP = -1$ whereas for pure LH states it gives $DOLP = 0.6$.

2.2 Modeling of structure composition

The material distribution and geometry parameters are taken from previous studies [38]. The design of the structure's special parameters is based on a simplified model of the “effective” Al-content resulting from the capillarity-driven Al-Ga segregation at the sharp wedges of the. The ratio between “effective” and “nominal” Al content:

$$x_{eff} = \frac{x}{x + K(1-x)} \quad (1)$$

where x is the nominal (bulk) Al concentration. For different arias of the pyramidal nanostructure K parameter is unique, so $K=8.9$ for the central QWR region and $K=2.1$ for side QWs [24]. Since the x_{eff} in an Al content, by definition, is associated with QWR spectral line [38], it leads to an overestimation of actual Al by the blue shift of ~ 30 meV (or $\sim 2\%$ Al content). The overestimation is constant in all points of QWR; thus, it does not affect CB or VB structure. This statement is consistent with experimental results. Effective Al content permits calculating the bandgap profile of the corresponding components of the 3D pyramidal heterostructure. In this paper, we implement one more assumption, due to similar Al content to the bulk, we neglect LQWs regions (blue color in Figure 1(a)), assuming Al content to be the same as in the bulk. More geometry details and the ratio of material distribution are also well described in previous studies [38] [35]. The bandgap dependence over Al content in GaAs is known from the literature [46]:

$$E_g (Al_x Ga_{1-x} As) = (1-x) E_g (GaAs) + x E_g (AlAs) - x(1-x)C \quad (2)$$

where C is the bowing parameter, $E_g(\text{GaAs}) = 1.519 \text{ eV}$ and $E_g(\text{AlAs}) = 3.1 \text{ eV}$ (low temperature values). According to (2) each 1% of Al content gives $\sim 15 \text{ meV}$ to the band gap. The ratio between the CB and VB offsets was taken as $\Delta\text{CB}/\Delta\text{VB} \sim 67/33$ [47][48].

$\text{Al}_x\text{Ga}_{1-x}\text{As}$ [111] nanostructures in inverted pyramids are implemented in the code; however, users can set any 3D structure. The option to add In content to GaAs and correspondent Hamiltonian is also implemented. Note that $\text{In}_x\text{Ga}_{1-x}\text{As}$ compound is a material with internal strain, and the Hamiltonian presented above has to be modified. We do not deliver Hamiltonian with strain; however, it is also implemented in the code. The numerical solution of the Hamiltonian was performed by the finite difference method.

The example of the model structure geometry is presented in Figure 2, 10 nm thick GaAs QD embedded in AlGaAs barriers. The modeled area is $40 \times 40 \text{ nm}$ size is enough to make sure that border conditions (infinite barriers) do not have an effect on exciton structure in the area of interest. The calculation grid parameter is chosen as 0.1 nm for all simulation results presented in this paper. The diameter of the QD/QWR cylinders is kept at 18 nm . Figure 2 b illustrates the Al distribution in the ZX plane ($Y \sim 0$). Here we will remind the main numbers. The effective Al content in the core cylinder of the QD is $\sim 2.8\%$, and in the vertical barrier cylinders, it is $\sim 7.2\%$ (for 40% nominal Al content).

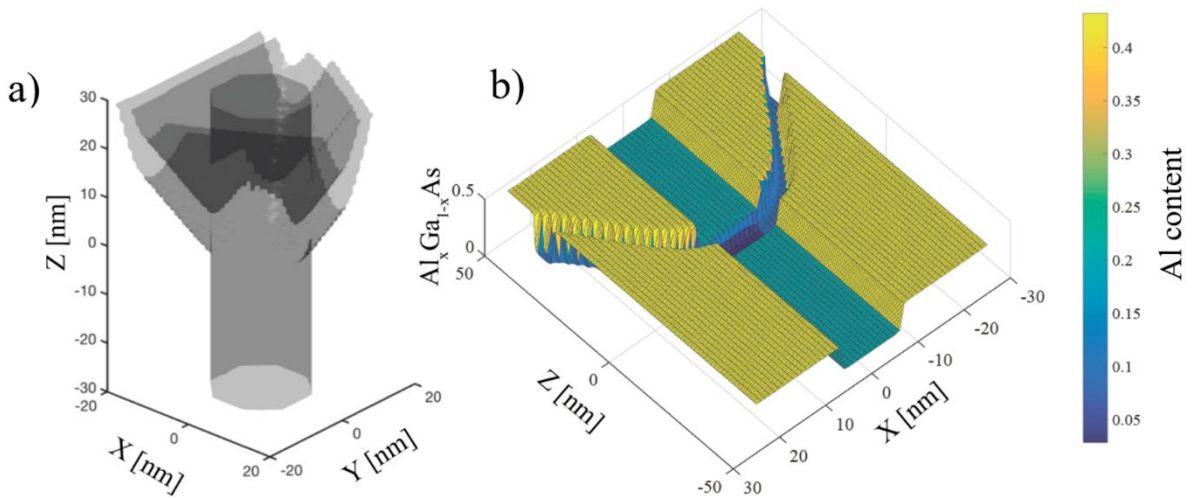


Figure 2. (a) 3D isosurface of Al content ($x=0.4$) in a simulated 10 nm thick GaAs QD nanostructure. (b) Z-X cut of the simulated nanostructure showing Al content distribution.

3. Results and discussion

3.1 LH and HH states evolution in QD

Figure 3 (a) presents the calculated confinement energies of the lowest CB and VB (Figure 3 (b)) states versus the QD thickness t , without Coulomb interaction. The height t of the QD cylinder (the QD “thickness”) is varied between 8 to 20 nm (see inset in Fig. 3(a)). The effective Al content in the core cylinder of the QD is $\sim 2.7\%$ (for 20% nominal Al content. In the vertical barrier cylinders, it is $\sim 7.2\%$ (for 40% nominal Al content), which is illustrated in Figure 3 (e)

$t \sim 13$ (see Figure 3 (b)). Remarkably, this transition also shows up in the VB mixing characteristic (Figure 3 (d)), where at the crossing point the HH and the LH WF portions are the same for the first two VB states. For $t < 13$ nm, the ground state is HH-like, with smaller t the structure behaves in this respect as a “thin” QD. For $t > 13$ nm, the ground state is LH-like, with larger t the structure behaves as a “QWR” or elongated QD. These results suggest the searching area to choose of QD parameters for achieving a structure at the border between HH and LH behavior of the VB ground state. To achieve more accurate results, the Coulomb interaction must be taken into account.

The calculated polarization-resolved optical spectra of this QD structure are shown in Figure 3 (c) for various thicknesses t ; red and blue curves correspond to linear polarization normal and parallel to the growth direction. Figure 3 (e) schematically presents light polarization axes with respect to the nanostructure. Line broadening of 2 meV was applied, and Coulomb interaction was taken into account as a perturbation. This set of spectra shows how the GS transition gradually changes its character from LH to HH with a reduction of QD thickness. Interestingly, the switching from HH to LH – like lowest energy state occurs near $t = 14$ nm (as in Figure 3(b)), which is different on 1nm from switching simulated without coulomb interaction.

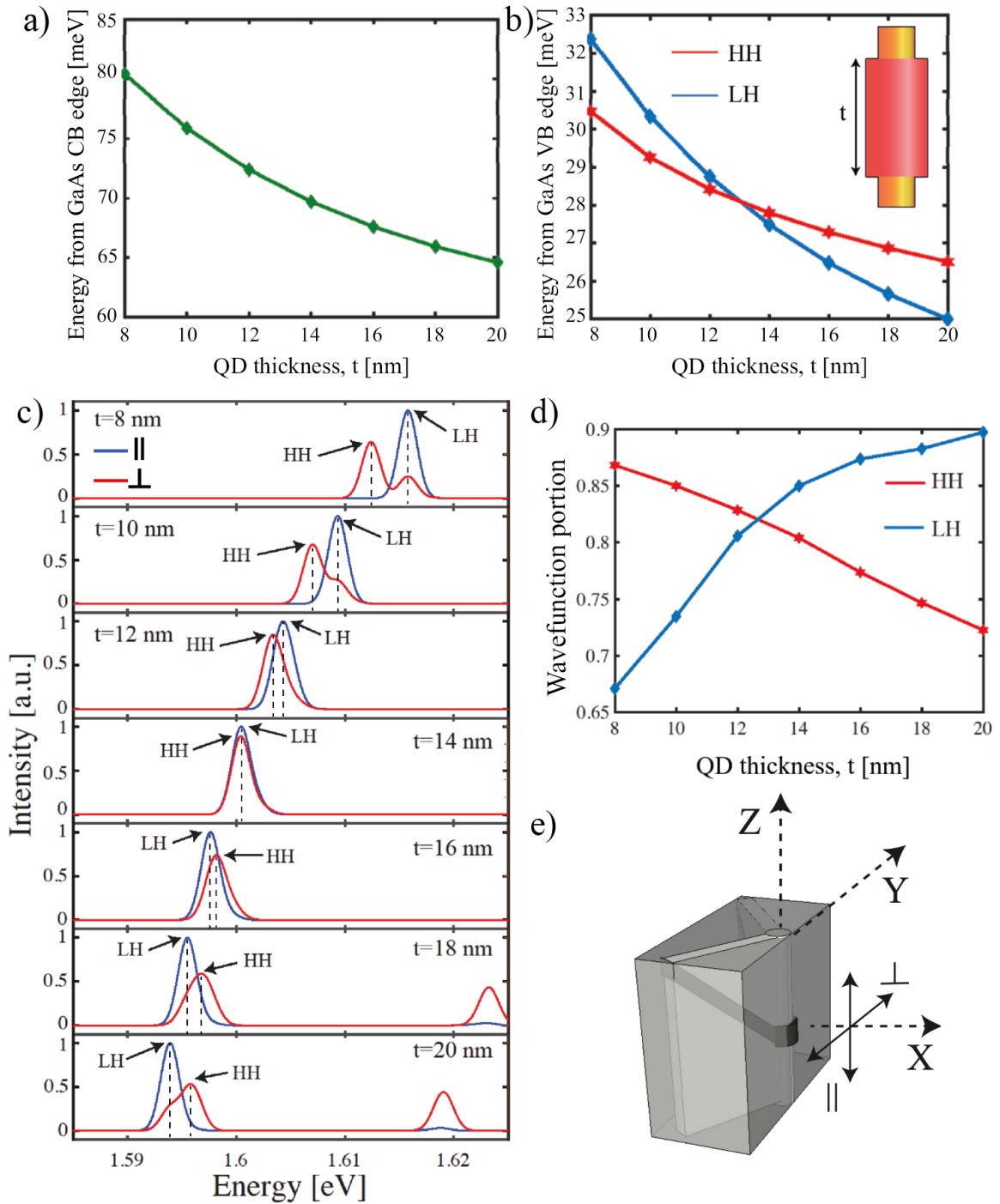


Figure 3. (a) Calculated dependence of energy of first CB state from QD thickness. (b) Calculated dependence of energy of first two VB states from QD thickness. Blue color corresponds to LH transitions, and red color to HH transitions. (c) Calculated absorption spectra of $t=8$ nm, 10 nm, 12 nm, 14 nm, 16 nm, 18 nm, 20 nm QD thickness. Different colors correspond to different polarizations. Blue is emission polarized in the Z direction and red in the XY plane. (d) Calculated wavefunction portions of the first two VB states from QD thickness. The red color is the state with HH, and another one by the blue color with LH major parts. (e) Schematic illustration of QD in an inverted pyramid with the indication of parallel and perpendicular light polarization.

We see that in a range of $t \sim 14$ nm, the QD GS transition changes its polarization with the switching of the VB ground state character from LH to HH. Since, around this point, small variations in the confinement potential can yield such GS character switching, such QD can serve as a base for achieving the desired dynamic transition using an electric field. Here we analyze the effect of an electric field on such “equilibrium”: QD structure.

To illustrate the effect of an electric field, we consider the same QD structure discussed above with fixed QD thickness at $t = 14$ nm. The confined CB and VB states are then computed by adding an electric field E oriented in the growth direction z . From the experimental point of view, considering the structure size of $L < 1\mu m$ the voltage magnitude at $T = 10K$ that can be applied is about 3V, give us a feasible range of electric field simulation up to $E_{\max} = 30000$ [V/cm].

Figure 4 (a) shows the calculated optical spectra of the QD structure for an electric field of amplitude $E = 20000$ [V/cm], oriented along the growth direction. We would like to highlight two significant differences compared to the spectrum for $E = 0$. First, the absorption edge is red-shifted due to a quantum confined Stark effect [13]. Secondly, the lowest energy transition line with nearly equal H and V light intensity components develops for $E > 0$ into a richer structure with characteristic polarization features. This is illustrated by DOLP spectrum, which shows an HH-like feature at low energies instead of $DOLP \sim 0$ for $E = 0$. The reason is the electric field that changes the QD potential profile in such way that the lowest VB state becomes HH-like, and the Stark shifts are different for the different VB states. Thus, applying an electric field can dynamically tune the QD structure to change the polarization state of light emitted by the QD ground states. The impact of the electric field on the lowest transition states energy is displayed on the right panel of Figure 4. The spectral lines near 1.595eV in Figure 4 are related to the first CB and first two VB transitions. Note that the polarization is determined by the part (LH or HH) of the VB wavefunction that best overlaps with the CB state.

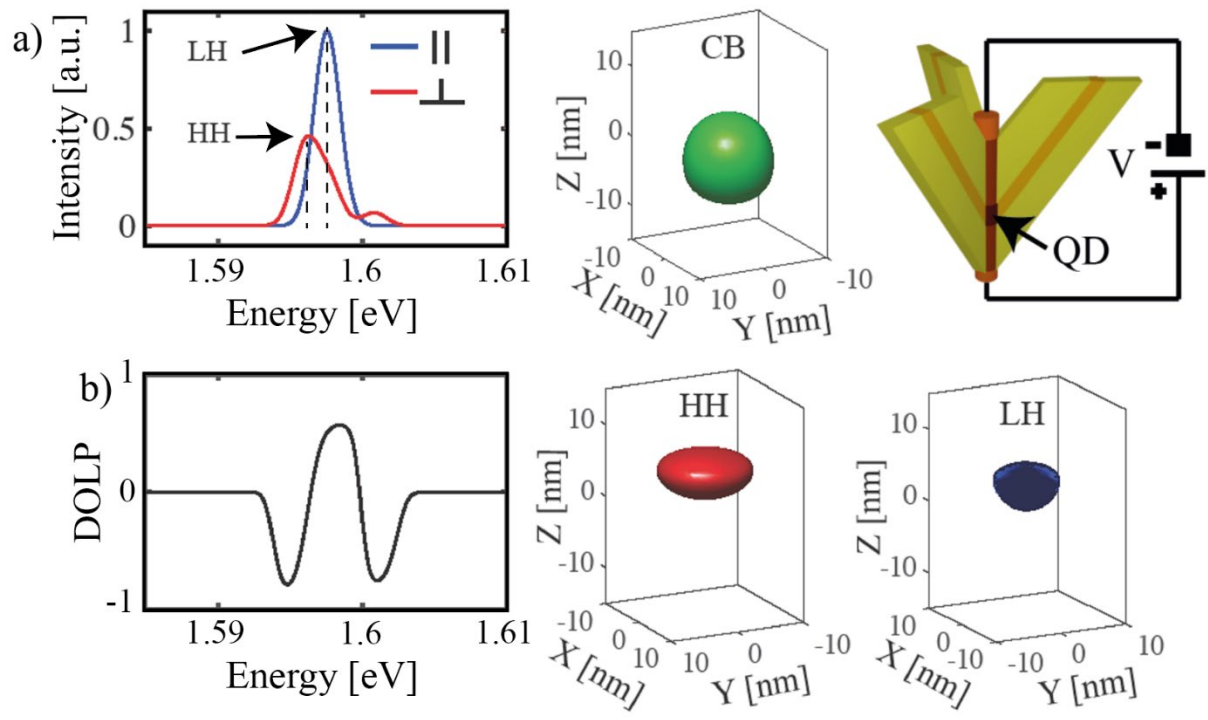


Figure 4. QD ($t=14$ nm), subject to an electric field $E=20000$ V/cm, applied in the z direction. Left panel: (a) Calculated optical spectra taking into account Coulomb interaction and 2 meV broadening. (b) DOLP spectra. Right panel: schematic presentation of QD in an inverted pyramid with electric contact and wavefunctions iso-surfaces of the GS CB state and parts of two lowest VB states that overlap with GS CB: green – electron; red – HH; blue - LH.

3.2 QDM Polarization control by barrier adjustment

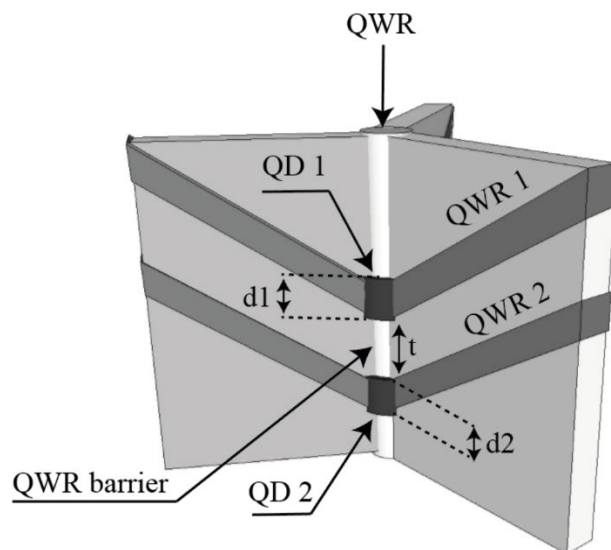


Figure 5. Schematic illustration of two QDs system (QD molecule) embedded in an inverted pyramid. The color illustrates the Al mole fraction in the different parties of the heterostructures.

QDM systems contain many parameters that affect QDs coupling strength, and thus system optical properties, the main geometrical parameters, are illustrated schematically in Figure 5. For example, here, we show the effect of barrier height on the polarization switching of the QDM GS emission. Figure 6 presents the dependence of the lowest CB and VB states on Al content (in ‘nominal’ values) in the outer barrier (nominal Al content in QD core: 20%; in external barriers: 40%, QD thickness $t = 7$ nm; barrier thickness $d = 5$ nm). The GS of the CB increases with increasing Al content as the potential energy of the barrier increases. The VB states dependence is more complex: in between the two extreme barrier heights, the VB GS changes its character from LH- to HH- like with increasing Al content (see Figure 6 b).

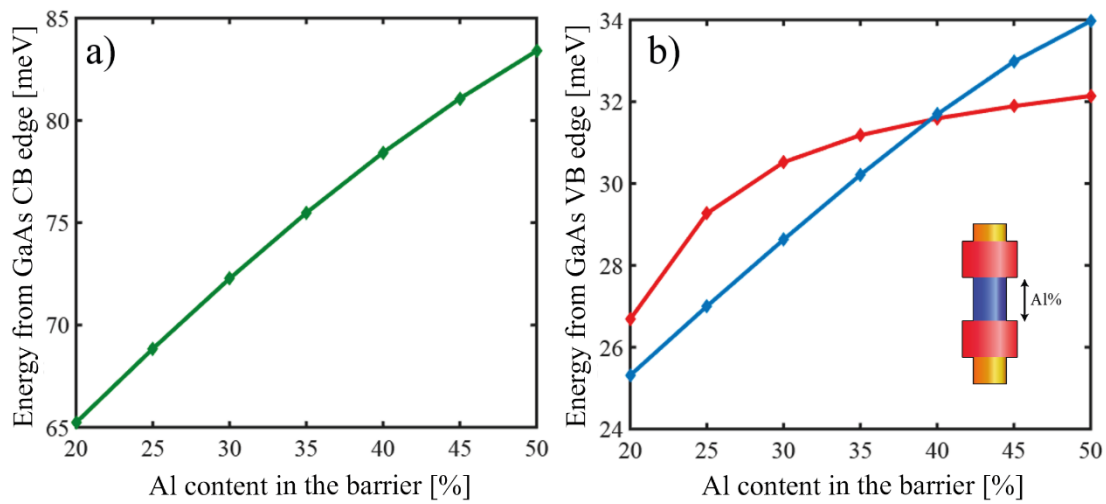


Figure 6. (a) Calculated energy dependence of the first CB state versus the QDM barrier composition (in ‘nominal’ values of Al content). (b) Calculated energy of the first two VB states from QD barrier composition. The blue line corresponds to LH transitions, red to HH transitions. The inset is a schematic of the QDM core part.

Figure 7 (a) summarizes the calculated optical spectra, considering Coulomb interaction as a perturbation and a line broadening of 2 meV. The lowest energy transition is mainly LH-like for low barriers and becomes degenerate with the HH-like one at $\sim 40\%$ Al. The spectra show the evolution of the HH and LH transition lines, their crossing when Al content becomes $\sim 40\%$, and at 50%, the complete change of the GS to HH one. Figure 7 (b) shows the spectral positions of the GS and the first excited transition versus the barrier Al content, indicating the VB character (red color for HH, blue for LH). Figure 7 (c) shows the VB mixing dependence on the barrier height. Summarizing, the common trend for all structures is that at certain inner QDs coupling regimes (from strong to low), the GS transition changes between LH to HH-like. As a consequence, the emission polarization of the GS also changes. This figure illustrates the two regimes of behavior, with two different GS transition types and polarization of emitted light.

The QDM system at the intermediate point where the HH and LH states are almost degenerate opens an opportunity to change the GS emission character dynamically by applying an external electric field due to the sensitivity of such structure.

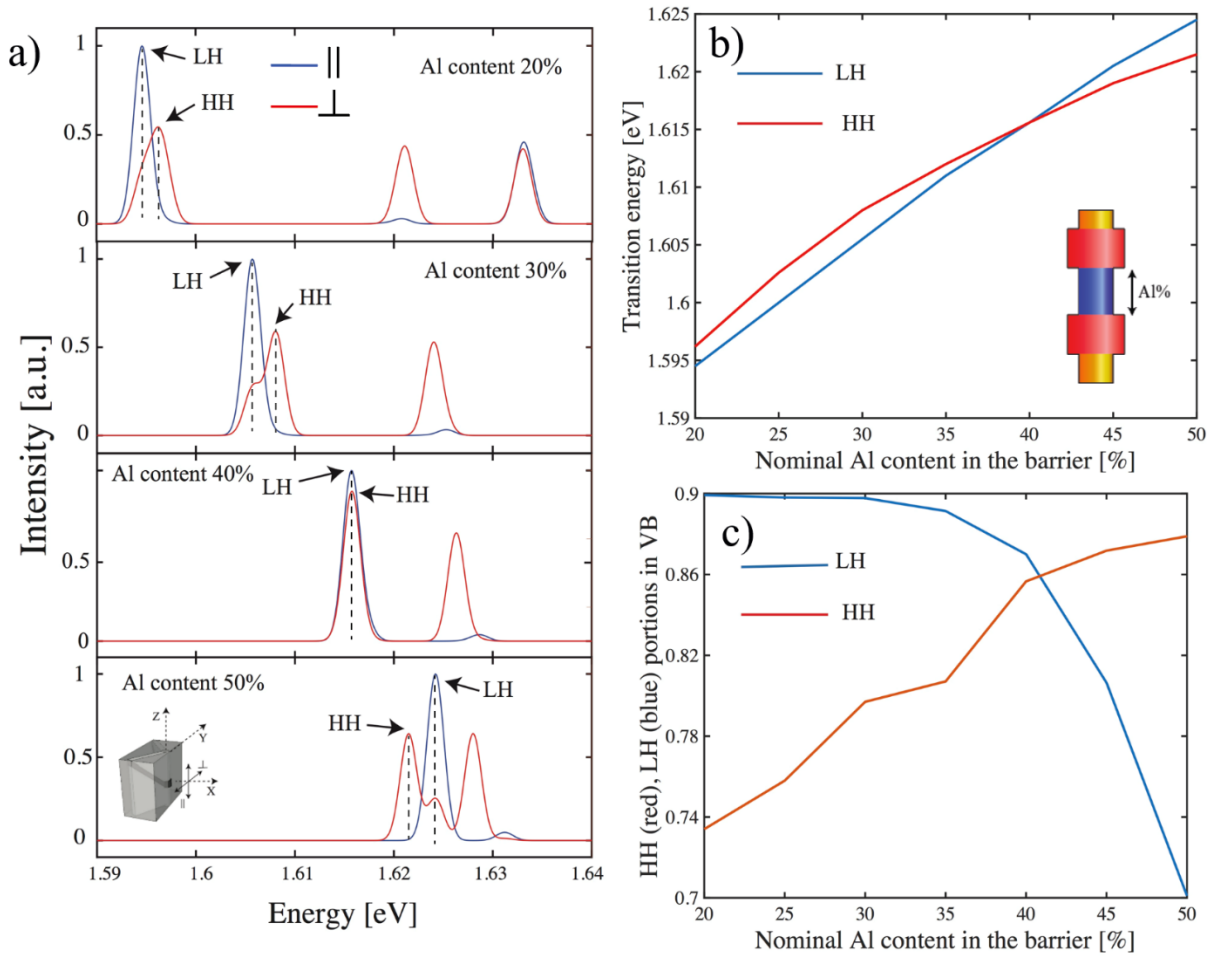


Figure 7. (a) Calculated absorption spectra of the QDM for different heights of the barrier (in 'nominal' values Al content). Lines corresponding to HH-like and LH-like transitions are indicated. (b) Calculated energies of the lowest energy transitions (a) versus QDM thickness barrier height. Different colors correspond to different transition types, the red line between CB and HH transition blue line between CB and LH transition. (c) Major wavefunction parts of the first two VB states dependence, HH - red and LH - blue.

Next, we consider the effect of an external electric field in a QDM with the following structural parameters: QD cores of 20% Al content and thickness $t = 7$ nm each, QD external barriers of 40% Al content, QD inner barrier thickness $d = 5$ nm and 35% Al content. Figure 8 shows the simulation results of the system without an external electric field ($E = 0$). Figure 8 (a) presents the calculated optical spectra, and Figure 8 (b) the corresponding DOLP spectra. In this configuration, the GS LH and HH transition is almost at the same energy, with a more complex structure of the excited states transitions. The right panel of Figure 8 shows a side view of the lowest CB and VB states WFs isosurfaces.

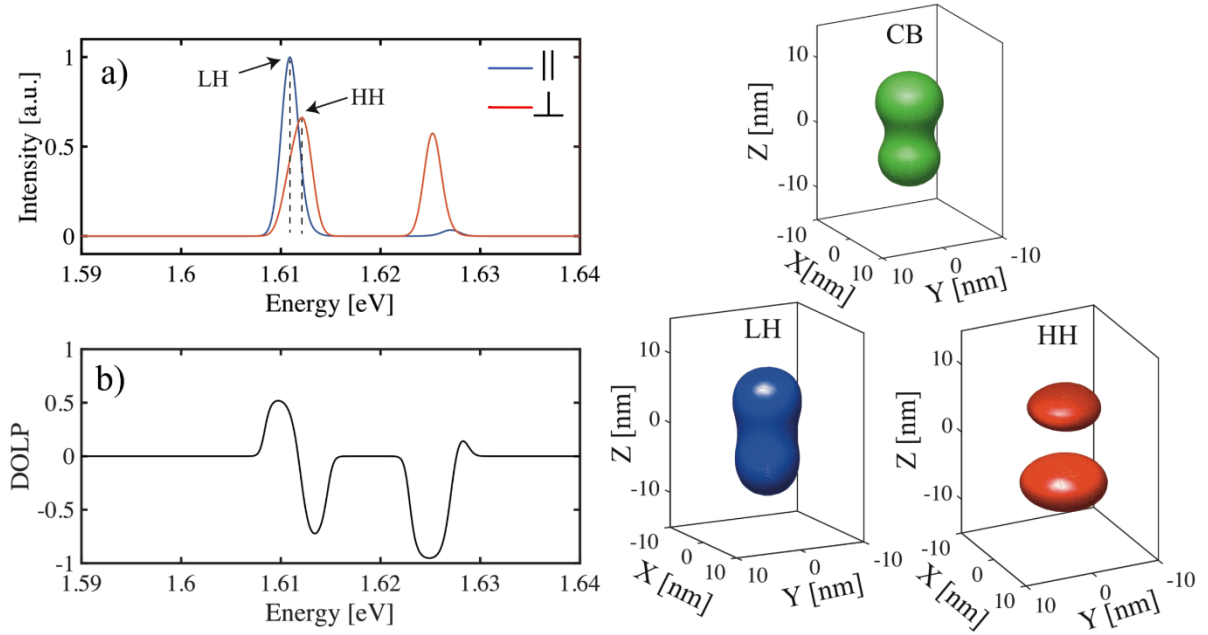


Figure 8. QDM structure (see text for parameters) without an electric field. Left panel: (a) Calculated absorption spectra taking into account Coulomb interaction and 2 meV broadening. (b) DOLP spectra. Right panel: wavefunctions iso-surfaces of the GS CB state and parts of two lowest VB states that overlap with GS CB: green – electron; red – HH; blue - LH.

For the same QDM structure, the other potential asymmetry induced by an external electric field of $E = 9000$ [V/cm] aligned in the growth direction dramatically changes the optical spectra and WFs shapes (Figure 9). As in the case of the single QD with the applied electric field, the polarization of the GS transition and its energy change. In contrast to the case $E = 0$, the lowest energy transition now has $DOLP = -0.6$ instead of $DOLP = 0.5$ to its more important HH character of the VB state involved. As usual, the electric field pushes the CB and VB WFs in the opposite direction for a Stark effect. This also leads to a reduction in the transition strength due to the smaller WF overlaps.

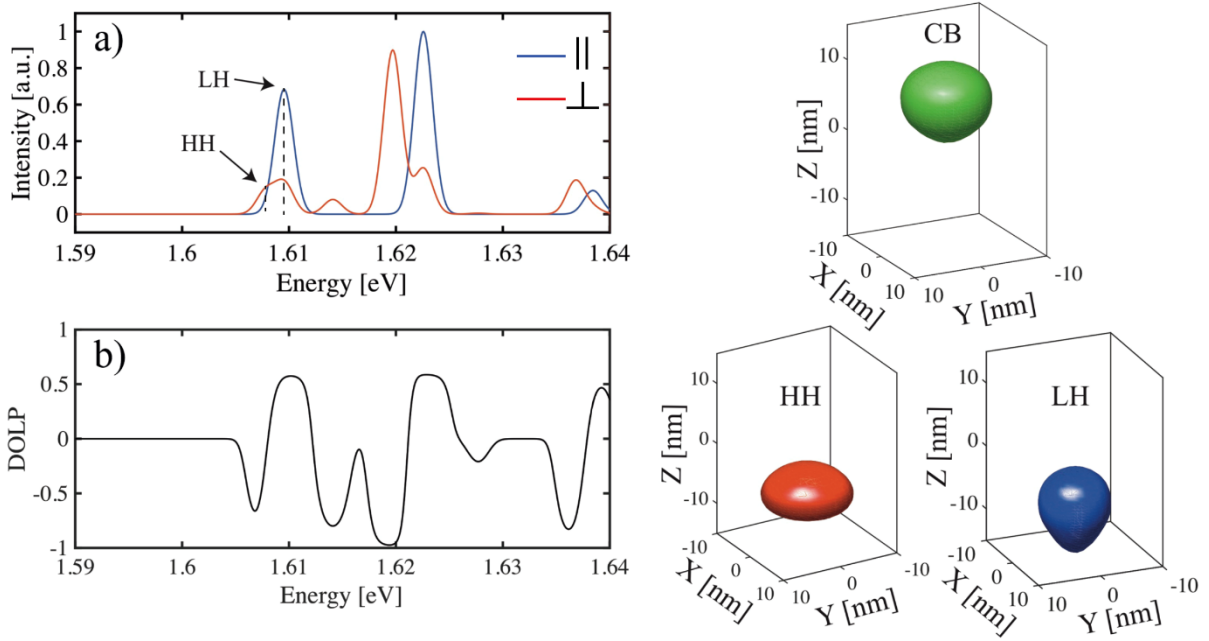


Figure 9. QDM structure (see text for parameters) subject to an electric field $E=9000$ V/cm, applied in the $+z$ direction. Left panel: (a) Calculated absorption spectra taking into account Coulomb interaction and 2 meV broadening. (b) DOLP spectra. Right panel: wavefunctions iso-surfaces of the GS CB state and parts of two lowest VB states that overlap with GS CB: green – electron; red – HH; blue - LH.

The case of two-QDs molecule can be extended to N QDs (QDSLs), which leads us to the formation of minibands [49], as was also shown in the case of QW superlattices [50]. Such systems can also be realized experimentally in inverted pyramids as a vertically aligned coupled QD array. In QDSLs, the barriers' height and width are crucial parameters that define the coupling strength between the QDs. In such systems with modulated internal potential in a low coupling regime, GS HH WFs can have as large as LH WF in QDs with flat potential. However, the corresponding emission will have a different polarization. The consequence of low coupling is that a "forest" of close-spaced optical transition lines appears. Under the application of an electric field, the excited CB and VB WFs overlap due to tunneling to neighbor QDs, while the first CB and VB states are separate and do not overlap [51]. From an experimental point of view, it's hard to fabricate and analyze the VB structure of N QDs due to structural complexity, optical line merging, and non-linear effects during the nanostructure growth.

4. Conclusion

The sensitivity of VB state structure to the environment of QD and QDM makes them good candidates for polarization-controlled single photon sources. A number of QDs were simulated by 4-band Luttinger–Kohn $\mathbf{k}\mathbf{p}$ model with QDs thickness from 8 nm and 23 nm in length. The “equilibrium” point where LH and HH have the same energy positions was found between ~ 14 nm long QD. Applying an electric field along the QD allows us to control the VB structure so that VB GS character becomes HH or LH; which can be observed experimentally by measuring DOLP. Modulating the coupling strength in QDM by the potential variations in the barrier between the QDs we study QDM sensitivity of optical properties to its structural parameters. We show that

QDMs are more sensitive to an external electric field than single QDs and demonstrate how it affects QDM absorption spectra. This knowledge will be helpful for the construction of future polarization-switching devices.

The model source code may be useful for similar studies or educational purposes. The code is available on Github: <https://github.com/Mikelazarev/Low-dimensional-band-structure-model>

5. Acknowledgment

My acknowledgments go to Prof. Fredrik Karlsson for providing numerical codes. Also, I would like to thank Prof. Eli Kapon for the useful discussions.

6. Appendix

The Hamiltonian in matrix form, taking into account SO interaction, looks like this:

$H = H_0 + H' + H^{SO}$ where:

$$H_0 = \begin{pmatrix} H_1 & 0 \\ 0 & H_1 \end{pmatrix} \text{ where } H_1 = \begin{pmatrix} E_c + \varepsilon & iP_0k_x & iP_0k_y & iP_0k_z \\ -iP_0k_x & E_v + \varepsilon & 0 & 0 \\ -iP_0k_y & 0 & E_v + \varepsilon & 0 \\ -iP_0k_z & 0 & 0 & E_v + \varepsilon \end{pmatrix}$$

$$H^{SO} = \frac{\Delta_0}{3} \begin{pmatrix} 0 & 0 & 0 & 0 & 0 & 0 & 0 & 0 \\ 0 & 0 & -i & 0 & 0 & 0 & 0 & 1 \\ 0 & i & 0 & 0 & 0 & 0 & 0 & 0 \\ 0 & 0 & 0 & 0 & 0 & -1 & i & 0 \\ 0 & 0 & 0 & 0 & 0 & 0 & 0 & 0 \\ 0 & 0 & 0 & -1 & 0 & 0 & i & 0 \\ 0 & 0 & 0 & -i & 0 & -i & 0 & 0 \\ 0 & 1 & i & 0 & 0 & 0 & 0 & 0 \end{pmatrix}$$

$$H' = \begin{pmatrix} H_2 & 0 \\ 0 & H_2 \end{pmatrix} \text{ where}$$

$$H_2 = \begin{pmatrix} 0 & 0 & 0 & 0 \\ 0 & L'k_x^2 + Mk_y^2 + Mk_z^2 & N'k_yk_x & N'k_zk_x \\ 0 & N'k_yk_x & Mk_x^2 + L'k_y^2 + Mk_z^2 & N'k_yk_z \\ 0 & N'k_zk_x & N'k_zk_y & Mk_x^2 + Mk_y^2 + L'k_z^2 \end{pmatrix}$$

A', B, L', M, N' are second order interactions due to Löwdin renormalization involving states outside the S, P subspace. $\varepsilon = \frac{\hbar^2 k^2}{2m_0}$ and Δ_0 is the spin-orbit splitting:

$$\Delta_0 = \frac{-3i\hbar}{4m_0c^2} \langle X | \frac{\partial V}{\partial x} p_y - \frac{\partial V}{\partial y} p_x | Y \rangle. \text{ In case of GaAs, } B=0.$$

This Hamiltonian contains four atomic bands, kinetic, spin-orbit, perturbation of five next bands, and atomic potential in terms of mean-field. Because the transition rate is proportional to $\langle \varphi_{cb} | e \cdot p | \varphi_{vb} \rangle$ where P is momentum e is a polarization vector. For optical studies, it's more convenient to change the basis of this Hamiltonian to the basis of eigenfunctions of the momentum operator (HH and LH basis). A set of new basis wavefunctions are presented in the following Table 1 [52].

Eigenvalues and corresponding eigenstates at $\mathbf{k} = 0$.			
Energy	First Kramers Set	Second Kramers Set	Name
E_c	$ \frac{1}{2}, -\frac{1}{2}\rangle = S \downarrow\rangle$	$ \frac{1}{2}, \frac{1}{2}\rangle = S \uparrow\rangle$	Electron
E'_v	$ \frac{3}{2}, \frac{3}{2}\rangle = \frac{i}{\sqrt{2}} (X + iY) \uparrow\rangle$	$ \frac{3}{2}, -\frac{3}{2}\rangle = \frac{-i}{\sqrt{2}} (X - iY) \downarrow\rangle$	Heavy Hole
E'_v	$ \frac{3}{2}, \frac{1}{2}\rangle = \frac{-i}{\sqrt{6}} (X + iY) \downarrow - 2Z \uparrow\rangle$	$ \frac{3}{2}, -\frac{1}{2}\rangle = \frac{i}{\sqrt{6}} (X - iY) \uparrow + 2Z \downarrow\rangle$	Light Hole
$E'_v - \Delta_0$	$ \frac{1}{2}, \frac{1}{2}\rangle = \frac{-i}{\sqrt{3}} (X + iY) \downarrow + Z \uparrow\rangle$	$ \frac{1}{2}, -\frac{1}{2}\rangle = \frac{-i}{\sqrt{3}} (X - iY) \uparrow - Z \downarrow\rangle$	SO Hole

Table 1 Eigenvalues and corresponding eigenstates of the CB and VB states.

New matrix elements in this basis looks like:

$$H_0 = \begin{pmatrix} E_c + \varepsilon & 0 & V & 0 & \sqrt{3}V^* & -\sqrt{2}U & -U & \sqrt{2}V \\ 0 & E_c + \varepsilon & -\sqrt{2}U & -\sqrt{3}V & 0 & -V^* & \sqrt{2}V^* & U \\ V^* & -\sqrt{2}U^* & E_v & 0 & 0 & 0 & 0 & 0 \\ 0 & -\sqrt{3}V^* & 0 & E_v & 0 & 0 & 0 & 0 \\ \sqrt{3}V^* & 0 & 0 & 0 & E_v & 0 & 0 & 0 \\ -\sqrt{2}U^* & -V & 0 & 0 & 0 & E_v & 0 & 0 \\ -U^* & \sqrt{2}V & 0 & 0 & 0 & 0 & E_v & 0 \\ \sqrt{2}V^* & U^* & 0 & 0 & 0 & 0 & 0 & E_v \end{pmatrix}$$

$$H^{SO} = \frac{\Delta_0}{3} \begin{pmatrix} 0 & 0 & 0 & 0 & 0 & 0 & 0 & 0 \\ 0 & 0 & 0 & 0 & 0 & 0 & 0 & 0 \\ 0 & 0 & 1 & 0 & 0 & 0 & 0 & 0 \\ 0 & 0 & 0 & 1 & 0 & 0 & 0 & 0 \\ 0 & 0 & 0 & 0 & 1 & 0 & 0 & 0 \\ 0 & 0 & 0 & 0 & 0 & 1 & 0 & 0 \\ 0 & 0 & 0 & 0 & 0 & 0 & -2 & 0 \\ 0 & 0 & 0 & 0 & 0 & 0 & 0 & -2 \end{pmatrix}$$

$$H' = \begin{pmatrix} 0 & 0 & 0 & 0 & 0 & 0 & 0 & 0 \\ 0 & 0 & 0 & 0 & 0 & 0 & 0 & 0 \\ 0 & 0 & -P+Q & -S^* & R & 0 & \sqrt{3/2}S & -\sqrt{2}Q \\ 0 & 0 & -S & -P-Q & 0 & R & -\sqrt{2}R & \sqrt{1/2}S \\ 0 & 0 & R^* & 0 & -P-Q & 0 & \sqrt{1/2}S^* & \sqrt{2}R^* \\ 0 & 0 & 0 & R^* & 0 & -P+Q & \sqrt{2}Q & \sqrt{3/2}S^* \\ 0 & 0 & \sqrt{3/2}S^* & -\sqrt{2}R^* & \sqrt{1/2}S & \sqrt{2}Q & -P & 0 \\ 0 & 0 & -\sqrt{2}Q & \sqrt{1/2}S^* & \sqrt{2}R & \sqrt{3/2}S & 0 & -P \end{pmatrix}$$

$$\text{Where: } \varepsilon = \frac{\hbar^2 k^2}{2m_0}, U = \frac{P_0}{\sqrt{3}} k_z, V = \frac{P_0}{\sqrt{6}} (k_x + ik_z), P = \frac{\hbar^2}{2m_0} \gamma_1 (k_x^2 + k_y^2 + k_z^2),$$

$$Q = \frac{\hbar^2}{2m_0} \gamma_2 (k_x^2 + k_y^2 - 2k_z^2), S = 2\sqrt{3} \frac{\hbar^2}{2m_0} \gamma_3 (k_x k_z - ik_y k_z),$$

$$R = -\sqrt{3} \frac{\hbar^2}{2m_0} (\gamma_2 (k_x^2 - k_y^2) - 2i\gamma_3 k_x k_y), \gamma_1 = -\frac{2}{3} \frac{m_0}{\hbar^2} (L' + 2M) - 1, \gamma_2 = -\frac{1}{3} \frac{m_0}{\hbar^2} (L' - M),$$

$$\gamma_3 = -\frac{1}{3} \frac{m_0}{\hbar^2} N'.$$

Where Δ is spin-orbit splitting and $\gamma_1, \gamma_2, \gamma_3$ is Luttinger parameters [53]. In the case of GaAs $\gamma_1 = 6.98$ $\gamma_2 = 2.06$ $\gamma_3 = 2.93$ [46]. In constant media, Luttinger parameters do not depend on coordinates. In the GaAs media case, effective masses of light and heavy holes depend on the direction of hole propagation. In case of $\text{Al}_x\text{Ga}_{1-x}\text{As}$ Luttinger parameters are chosen as a linear interpolation between the GaAs and AlAs. In AlAs, Luttinger parameters $\gamma_1 = 3.76$, $\gamma_2 = 0.82$, $\gamma_3 = 1.42$.

The Luttinger Hamiltonian we discussed so far is written in the x, y, and z directions corresponding to the principal crystallographic directions [hhe]. We consider structures with modulated potential along the z [111] direction. Thus, the Hamiltonian needs to be rewritten to

a new basis. Since SO and CB bands are far from LH and HH for simplicity, and we decouple them. Thus, the 3D Schrodinger equation with effective mass for conduction band electrons can be solved separately from Luttinger Hamiltonian for VB. The Luttinger Hamiltonian, in a new basis, looks like [54]:

$$H = \begin{pmatrix} D_{HH} & -S & R & 0 \\ -S^* & D_{LH} & 0 & R \\ R^* & 0 & D_{LH} & S \\ 0 & R^* & S^* & D_{HH} \end{pmatrix}$$

Where

$$\begin{aligned} D_{HH} &= -\frac{\hbar}{2m_e} \left[\frac{\partial}{\partial x} (\gamma_1 + \gamma_3) \frac{\partial}{\partial x} + \frac{\partial}{\partial y} (\gamma_1 + \gamma_3) \frac{\partial}{\partial y} + \frac{\partial}{\partial z} (\gamma_1 - 2\gamma_3) \frac{\partial}{\partial z} \right] + V \\ D_{LH} &= -\frac{\hbar}{2m_e} \left[\frac{\partial}{\partial x} (\gamma_1 - \gamma_3) \frac{\partial}{\partial x} + \frac{\partial}{\partial y} (\gamma_1 - \gamma_3) \frac{\partial}{\partial y} + \frac{\partial}{\partial z} (\gamma_1 + 2\gamma_3) \frac{\partial}{\partial z} \right] + V \\ R &= \frac{\hbar}{2m_e} \sqrt{3} \left[\frac{\partial}{\partial x} \left(\frac{2\gamma_3 + \gamma_2}{3} \right) \frac{\partial}{\partial x} - \frac{\partial}{\partial y} \left(\frac{2\gamma_3 + \gamma_2}{3} \right) \frac{\partial}{\partial y} - i \frac{\partial}{\partial x} \left(\frac{2\gamma_3 + \gamma_2}{3} \right) \frac{\partial}{\partial y} - i \frac{\partial}{\partial y} \left(\frac{2\gamma_3 + \gamma_2}{3} \right) \frac{\partial}{\partial x} \right] + \\ &+ \frac{\hbar}{m_e} \frac{2}{\sqrt{6}} \left[\frac{\partial}{\partial x} (\gamma_3 - \gamma_2) \frac{\partial}{\partial z} + \frac{\partial}{\partial z} (\gamma_3 - \gamma_2) \frac{\partial}{\partial x} + i \frac{\partial}{\partial y} (\gamma_3 - \gamma_2) \frac{\partial}{\partial z} + i \frac{\partial}{\partial z} (\gamma_3 - \gamma_2) \frac{\partial}{\partial y} \right] \\ S &= -\frac{\hbar}{2m_e} \sqrt{3} \left[\frac{\partial}{\partial x} \left(\frac{\gamma_3 + 2\gamma_2}{3} \right) \frac{\partial}{\partial z} + \frac{\partial}{\partial z} \left(\frac{\gamma_3 + 2\gamma_2}{3} \right) \frac{\partial}{\partial x} - i \frac{\partial}{\partial y} \left(\frac{\gamma_3 + 2\gamma_2}{3} \right) \frac{\partial}{\partial z} - i \frac{\partial}{\partial z} \left(\frac{\gamma_3 + 2\gamma_2}{3} \right) \frac{\partial}{\partial y} \right] - \\ &- \frac{\hbar}{2m_e} \sqrt{\frac{2}{3}} \left[\frac{\partial}{\partial x} (\gamma_3 - \gamma_2) \frac{\partial}{\partial x} - \frac{\partial}{\partial y} (\gamma_3 - \gamma_2) \frac{\partial}{\partial y} + i \frac{\partial}{\partial x} (\gamma_3 - \gamma_2) \frac{\partial}{\partial y} + i \frac{\partial}{\partial y} (\gamma_3 - \gamma_2) \frac{\partial}{\partial x} \right] \end{aligned}$$

7. References

- [1] K. W. J. Barnham *et al.*, “Quantum well solar cells,” *Phys. E Low-Dimensional Syst. Nanostructures*, vol. 14, no. 1–2, pp. 27–36, 2002, doi: 10.1016/S1386-9477(02)00356-9.
- [2] S. Nakamura, M. Senoh, N. Iwasa, and S. I. Nagahama, “High-power InGaN single-quantum-well-structure blue and violet light-emitting diodes,” *Appl. Phys. Lett.*, vol. 67, no. 1995, p. 1868, 1995, doi: 10.1063/1.114359.
- [3] Z. I. Alferov, “Nobel lecture: The double heterostructure concept and its applications in physics, electronics, and technology,” *Rev. Mod. Phys.*, vol. 73, no. 3, pp. 767–782, 2001, doi: 10.1103/RevModPhys.73.767.
- [4] B. F. Levine, “Quantum-well infrared photodetectors,” *J. Appl. Phys.*, vol. 74, no. 8, 1993, doi: 10.1063/1.354252.

- [5] F. H. Rau, B., P. Waltereit, O. Brandt, M. Ramsteiner, K. H. Ploog, J. Puls, “In-plane polarization anisotropy of the spontaneous emission of M -plane GaN/(Al, Ga) N quantum wells,” *Appl. Phys. Lett.*, vol. 77, 2000.
- [6] F. Vouilloz, D. Y. Oberli, M. A. Dupertuis, A. Gustafsson, F. Reinhardt, and E. Kapon, “Polarization anisotropy and valence band mixing in semiconductor Quantum wires,” *Phys. Rev. Lett.*, vol. 78, no. 8, pp. 1580–1583, 1997, doi: 10.1103/PhysRevLett.78.1580.
- [7] M. Davanco *et al.*, “Heterogeneous integration for on-chip quantum photonic circuits with single quantum dot devices,” *Nat. Commun.*, 2017, doi: 10.1038/s41467-017-00987-6.
- [8] C. P. Dietrich, A. Fiore, M. G. Thompson, M. Kamp, and S. Ofling, “GaAs integrated quantum photonics: Towards compact and multi-functional quantum photonic integrated circuits,” *Laser Photon. Rev.*, 2016, Accessed: Apr. 19, 2018. [Online]. Available: <https://arxiv.org/pdf/1601.06956.pdf>.
- [9] I. Söllner *et al.*, “Deterministic photon-emitter coupling in chiral photonic circuits,” *Nat. Nanotechnol.*, vol. 10, no. 9, pp. 775–778, 2015, doi: 10.1038/nnano.2015.159.
- [10] J. He *et al.*, “Growth, structural, and optical properties of self-assembled (In,Ga)As quantum posts on GaAs,” *Nano Lett.*, vol. 7, no. 3, pp. 802–806, 2007, doi: 10.1021/nl070132r.
- [11] L. Wang *et al.*, “Towards deterministically controlled InGaAs/GaAs lateral quantum dot molecules,” *New J. Phys.*, vol. 10, 2008, doi: 10.1088/1367-2630/10/4/045010.
- [12] Q. Zhu, K. F. Karlsson, E. Pelucchi, and E. Kapon, “Transition from two-dimensional to three-dimensional quantum confinement in semiconductor quantum wires/quantum dots,” *Nano Lett.*, vol. 7, no. 8, pp. 2227–2233, 2007, doi: 10.1021/nl0706650.
- [13] P. W. Fry *et al.*, “Inverted Electron-Hole Alignment in InAs-GaAs Self-Assembled Quantum Dots,” *Phys. Rev. Lett.*, vol. 84, no. 4, pp. 733–736, 2000, doi: 10.1103/PhysRevLett.84.733.
- [14] A. J. Bennett *et al.*, “Electric-field-induced coherent coupling of the exciton states in a single quantum dot,” *Nat. Phys.*, vol. 6, no. 12, pp. 947–950, 2010, doi: 10.1038/nphys1780.
- [15] J. Martín-, “Strain-tuning of the optical properties of semiconductor nanomaterials by integration onto piezoelectric actuators,” *Semicond. Sci. Technol.*, vol. 33, 2018, Accessed: Jun. 02, 2018. [Online]. Available: <http://iopscience.iop.org/article/10.1088/1361-6641/aa9b53/pdf>.
- [16] S. G. Carter *et al.*, “Quantum control of a spin qubit coupled to a photonic crystal cavity,” *Nat. Photonics*, vol. 7, no. 4, pp. 329–334, 2013, doi: 10.1038/nphoton.2013.41.
- [17] M. T. Rakher, N. G. Stoltz, L. A. Coldren, P. M. Petroff, and D. Bouwmeester, “Polarization-switchable single photon source using the Stark effect,” *Appl. Phys. Lett.*, vol. 93, no. 9, pp. 2008–2010, 2008, doi: 10.1063/1.2978396.

- [18] S. Reitzenstein and A. Forchel, “Quantum dot micropillars,” *J. Phys. D. Appl. Phys.*, vol. 43, no. 3, 2010, doi: 10.1088/0022-3727/43/3/033001.
- [19] J. Zhang *et al.*, “Single Photons On-Demand from Light-Hole Excitons in Strain-Engineered Quantum Dots,” *Nano Lett.*, 2014, doi: 10.1021/nl5037512.
- [20] S. M. Reimann and M. Manninen, “Electronic structure of quantum dots,” *Rev. Mod. Phys.*, vol. 74, no. 4, pp. 1283–1342, 2002, doi: 10.1103/RevModPhys.74.1283.
- [21] W. KOHN and L. J. SHAM, “Self-Consistent Equations Including Exchange and Correlation Effects,” *Phys. Rev.*, vol. 140, no. 5, 1965, [Online]. Available: <https://doi.org/10.1103/PhysRev.140.A1133>.
- [22] K. A. Mäder and A. Zunger, “Empirical atomic pseudopotentials for AlAs/GaAs superlattices, alloys, and nanostructures,” *Phys. Rev. B*, vol. 50, no. 23, pp. 17393–17405, 1994, doi: 10.1103/PhysRevB.50.17393.
- [23] T. B. Boykin, N. Kharche, G. Klimeck, and M. Korkusinski, “Approximate bandstructures of semiconductor alloys from tight-binding supercell calculations,” *J. Phys. Condens. Matter*, vol. 19, no. 3, 2007, doi: 10.1088/0953-8984/19/3/036203.
- [24] A. R. Kelsall RW, Taylor RI, Wood AC, “Hole transport and relaxation in the valence bands of GaAs/AlAs quantum well,” *Superlattices Microstruct.*, vol. 5, no. 2, pp. 207–211, 1989, doi: [https://doi.org/10.1016/0749-6036\(89\)90285-1](https://doi.org/10.1016/0749-6036(89)90285-1).
- [25] J. A. Majewski, M. Stadele, and P. Vogl, “Electronic structure of biaxially-strained wurtzite crystals GaN and AlN,” *Mater. Res. Soc. Symp. - Proc.*, vol. 449, pp. 887–892, 1997, doi: 10.1557/proc-449-887.
- [26] O. Marquardt, E. P. O’Reilly, and S. Schulz, “Electronic properties of site-controlled (111)-oriented zinc-blende InGaAs/GaAs quantum dots calculated using a symmetry-adapted $k \cdot p$ Hamiltonian,” *J. Phys. Condens. Matter*, vol. 26, no. 3, 2014, doi: 10.1088/0953-8984/26/3/035303.
- [27] Y. Kajikawa, “Optical anisotropy of (111)-oriented strained quantum-wells calculated with the effect of the spin-orbit split-off band,” *J. Appl. Phys.*, vol. 86, no. 10, pp. 5663–5677, 1999, doi: 10.1063/1.371577.
- [28] S. Tomić, A. G. Sunderland, and I. J. Bush, “Parallel multi-band $k \cdot p$ code for electronic structure of zinc blend semiconductor quantum dots,” *J. Mater. Chem.*, vol. 16, no. 20, pp. 1963–1972, 2006, doi: 10.1039/b600701p.
- [29] J. Andrzejewski, G. Sęk., E. O’Reilly, A. Fiore, and J. Misiewicz, “Eight-band $k \cdot p$ calculations of the composition contrast effect on the linear polarization properties of columnar quantum dots,” *J. Appl. Phys.*, vol. 107, no. 7, pp. 0–12, 2010, doi: 10.1063/1.3346552.
- [30] M. Gladysiewicz, R. Kudrawiec, J. M. Miloszewski, P. Weetman, J. Misiewicz, and M. S. Wartak, “Band structure and the optical gain of GaInNAs/GaAs quantum wells modeled within 10-band and 8-band $k \cdot p$ model,” *J. Appl. Phys.*, vol. 113, no. 6, 2013, doi: 10.1063/1.4790568.

- [31] Z. Song *et al.*, “Corrigendum: Band structure of Ge $1-x$ Sn x alloy: a full-zone 30-band kp model,” *New J. Phys.*, vol. 22, no. 1, p. 019502, 2020, [Online]. Available: <https://iopscience.iop.org/article/10.1088/1367-2630/ab6794>.
- [32] M. Gladysiewicz, R. Kudrawiec, and M. S. Wartak, “Theoretical studies of optical gain tuning by hydrostatic pressure in GaInNAs/GaAs quantum wells,” *J. Appl. Phys.*, vol. 115, no. 3, p. 033515, 2014, doi: 10.1063/1.4862230.
- [33] Q. Zhu *et al.*, “Hybridization of electron and hole states in semiconductor quantum-dot molecules,” *Small*, vol. 5, no. 3, pp. 329–335, 2009, doi: 10.1002/sml.200801214.
- [34] V. Troncale, K. F. Karlsson, E. Pelucchi, A. Rudra, and E. Kapon, “Control of valence band states in pyramidal quantum dot-in-dot semiconductor heterostructures,” *Appl. Phys. Lett.*, vol. 91, no. 24, pp. 45–48, 2007, doi: 10.1063/1.2820693.
- [35] M. Lazarev, A. Rudra, and E. Kapon, “Physical origins of optical anisotropy in quantum-confined semiconductors: The roles of valence band mixing, transition broadening, and state filling,” *J. Appl. Phys.*, vol. 133, no. 9, 2023, doi: 10.1063/5.0131958.
- [36] K. F. Karlsson *et al.*, “Optical polarization anisotropy and hole states in pyramidal quantum dots,” *Appl. Phys. Lett.*, vol. 89, no. 25, 2006, doi: 10.1063/1.2402241.
- [37] Q. Zhu *et al.*, “Pyramidal GaAs/ Al $_z$ Ga $1-z$ As quantum wire/dot systems with controlled heterostructure potential,” *Phys. Rev. B - Condens. Matter Mater. Phys.*, vol. 82, no. 16, pp. 1–13, 2010, doi: 10.1103/PhysRevB.82.165315.
- [38] Q. Zhu, E. Pelucchi, S. Dalessi, K. Leiter, M. A. Dupertuis, and E. Kapon, “Alloy segregation, quantum confinement, and carrier capture in self-ordered pyramidal quantum wires,” *Nano Lett.*, vol. 6, no. 5, pp. 1036–1041, 2006, doi: 10.1021/nl060066d.
- [39] J. Szeszko *et al.*, “Exciton confinement and trapping dynamics in double-graded-bandgap quantum nanowires,” *Appl. Phys. Lett.*, vol. 100, no. 21, pp. 0–4, 2012, doi: 10.1063/1.4721660.
- [40] V. Troncale, K. F. Karlsson, and E. Kapon, “Dynamic switching of hole character and single photon polarization using the quantum confined Stark effect in quantum dot-in-dot structures,” *Nanotechnology*, vol. 21, no. 28, 2010, doi: 10.1088/0957-4484/21/28/285202.
- [41] V. Troncale, “Tailored-Potential Pyramidal Quantum Dot Heterostructures,” *PhD thesis, EPFL*, vol. 4786, 2010, doi: 10.5075/EPFL-THESIS-4786.
- [42] L. Mikhail and K. Fredrik, “Low-dimensional semiconductor band structure model based on 4-band approximation k.p theory,” Dec. 2022, doi: 10.5281/ZENODO.7438050.
- [43] E. O. Kane, “Band structure of indium antimonide,” *J. Phys. Chem. Solids*, vol. 1, no. 4, pp. 249–261, 1957, doi: 10.1016/0022-3697(57)90013-6.
- [44] R. J. Warburton *et al.*, “Coulomb interactions in small charge-tunable quantum dots: A

- simple model,” *Phys. Rev. B*, vol. 58, no. 24, pp. 16221–16231, 1998, doi: 10.1103/PhysRevB.58.16221.
- [45] P. O. Löwdin, “A note on the quantum-mechanical perturbation theory,” *J. Chem. Phys.*, vol. 19, no. 11, pp. 1396–1401, 1951, doi: 10.1063/1.1748067.
- [46] I. Vurgaftman, J. R. Meyer, and L. R. Ram-Mohan, “Band parameters for III-V compound semiconductors and their alloys,” *J. Appl. Phys.*, vol. 89, no. 11 I, pp. 5815–5875, 2001, doi: 10.1063/1.1368156.
- [47] R. F. Kopf, M. H. Herman, M. L. Schnoes, A. P. Perley, G. Livescu, and M. Ohring, “Band offset determination in analog graded parabolic and triangular quantum wells of GaAs/AlGaAs and GaInAs/AlInAs,” *J. Appl. Phys.*, vol. 71, no. 10, pp. 5004–5011, 1992, doi: 10.1063/1.350600.
- [48] W. Langbein, H. Gislason, and J. M. Hvam, “Optimization of the confinement energy of quantum-wire states in T-shaped GaAs/Al(x)Ga(1-x)As structures,” *Phys. Rev. B*, vol. 54, no. 20, pp. 14595–14603, 1996, doi: 10.1103/PhysRevB.54.14595.
- [49] T. Sugaya, T. Amano, M. Mori, and S. Niki, “Miniband formation in InGaAs quantum dot superlattice,” *Appl. Phys. Lett.*, vol. 97, no. 4, pp. 2010–2013, 2010, doi: 10.1063/1.3470108.
- [50] R. Dingle and etc., “Direct Observation of Superlattice Formation in a Semiconductor Heterostructure,” *Phys. Rev. Lett.*, vol. 34, no. 21, pp. 1327–1330, 1975.
- [51] M. Lazarev, “Tailored-Potential Semiconductor Quantum Nanostructures Grown in Inverted Pyramids,” *PhD Theses, Lausanne, EPFL*, 2019, doi: <https://doi.org/10.5075/epfl-thesis-9461>.
- [52] J. H. Davies, “The Physics of Low-Dimensional Semiconductors.” Cambridge University Press, 1998.
- [53] J. M. Luttinger and W. Kohn, “Motion of Electrons and Holes in Perturbed Periodic Fields,” *Phys. Rev.*, vol. 97, 1955, doi: 10.1103/PhysRev.97.869.
- [54] G. Fishman, “Hole subbands in strained quantum-well semiconductors in [hhk] directions,” *PRB*, vol. 52, 1995, Accessed: Nov. 22, 2017. [Online]. Available: <https://journals.aps.org/prb/pdf/10.1103/PhysRevB.52.11132>.